Fuel 235 (2019) 339–349

Contents lists available at ScienceDirect

Fuel

journal homepage: www.elsevier.com/locate/fuel

Full Length Article

Revisiting methane absolute adsorption in organic nanopores from molecular simulation and Ono-Kondo lattice model

Wanying Pang, Zhehui Jin*

School of Mining and Petroleum Engineering, Department of Civil and Environmental Engineering, University of Alberta, Edmonton, AB T6G 1H9, Canada

ARTICLE INFO

Keywords:
Absolute adsorption
Shale nanopore
Monte Carlo simulation
Ono-Kondo lattice model

ABSTRACT

Accurate characterization of methane absolute adsorption in shale plays an important role in estimation of gas-in-place and prediction of well productivity. Previously, methane adsorption in shale nanopores was considered as a single-layer structure. However, it has been shown that due to strong fluid-surface interactions, methane can form transition zone between the first adsorption layer and free gas phase. Such transition zone can negatively affect the accuracy of absolute adsorption estimation from excess adsorption, which is the mostly measured adsorption property in experiments. In this work, we use grand canonical Monte Carlo (GCMC) simulations to characterize the transition zone and propose a modified adsorption model. Based on the modified adsorption model, which can explicitly take into account the effect of transition zone, we use Ono-Kondo (OK) lattice model with multilayer structure to calculate the absolute adsorption in each layer and compare with GCMC simulations. The newly proposed OK model with multilayer structure only needs layer width as an input and calculates the density in each layer and subsequently the absolute adsorption by fitting the excess adsorption. While OK model can significantly reduce calculation time, discrepancy from GCMC simulation can be less than 6%. Our work should provide important insights into the accurate characterization of methane absolute adsorption from experimental measurement.

1. Introduction

Shale gas has become a very important unconventional energy resource and significantly increased global energy supply in the past decade [1–4]. Unlike conventional reservoirs, where hydrocarbon fluids are stored in large pores in the range of micrometers and hundreds of nanometers [5], significant amount of pores in shale reservoirs may be in the range of a few nanometers [6,7]. In small nanopores, hydrocarbon fluid properties are very different from bulk and surface adsorption plays an important role in the overall gas-in-place (GIP), which is one of key parameters to assess shale gas capacity [8]. As a result, the adsorbed gas in shale reservoir which behaves differently from free gas, may contribute 20%–85% of total shale gas content [1–3,8,9]. Thus, knowledge and understandings about adsorbed gas in shale play a key role in the accurate estimation of GIP and the prediction of well productivity.

Shale is composed of two distinct matters: organic and inorganic [6]. Organic matter, which mainly consists of kerogen, is reported to have a dominant contribution to methane adsorption capacity in shale [6,7,10–16]. In addition, large amount of nano-sized pores are present in clay minerals which are important constituents of inorganic matters [6,17], where gas adsorption can be significant [18]. While total organic carbon (TOC), maturity and kerogen type, specific surface area (SSA), moisture content, temperature and surface functional groups are controlling factors of adsorption behavior in organic matters [6,19], in clay nanopores, SSA, moisture content and temperature are dominant factors [18,20–22].

There have been a large number of experimental works to study gas adsorption behavior in shale media [23–27]. Among them, gravimetric and volumetric methods have been used to measure the Gibbs adsorption of various hydrocarbon species. Gravimetric method, which uses magnetic suspension balance to obtain adsorption isotherms [28], measures the excess adsorption capacity m_{ex} based on the difference between gravity and buoyancy [29]. On the other hand, volumetric method measures total gas uptake m_{tot} in porous media [30] and then, m_{ex} is obtained by subtracting the amount of bulk free gas in all accessible pore volume V_p from m_{tot} [31,32]. However, m_{ex} is different from absolute adsorption m_{abs}, which can describe the adsorbed gas capacity in shale.

Methane adsorption in nanopores is generally considered as a single-layer adsorption model [21,33]. In large nanopores, methane density distributions in the middle of pores are the same as bulk ρ_b [20],

* Corresponding author.
E-mail address: zhehui2@ualberta.ca (Z. Jin).

https://doi.org/10.1016/j.fuel.2018.07.098
Received 30 April 2018; Received in revised form 20 July 2018; Accepted 22 July 2018
Available online 01 August 2018
0016-2361/ © 2018 Elsevier Ltd. All rights reserved.

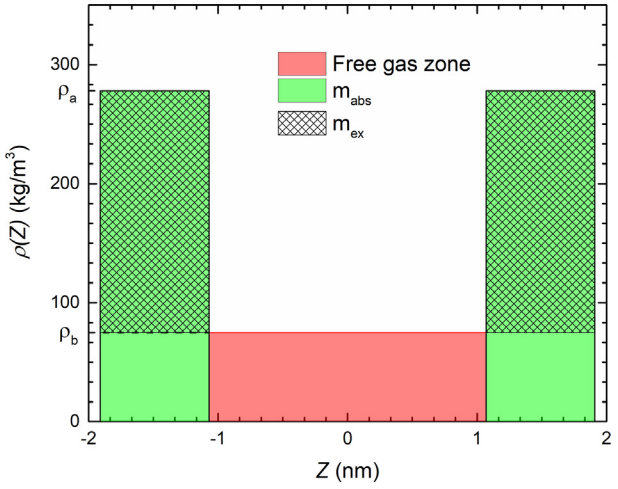

Fig. 1. Schematic representation of methane adsorption model based on single-layer adsorption assumption.

while in the vicinity of pore surfaces, they are very different [21]. Based on the single-layer adsorption model, methane adsorption in nanopores can be divided into adsorbed and free gas regions as shown in Fig. 1. m_{abs} is defined as the adsorbed amount in the adsorbed phase [34]. According to the adsorption model given in Fig. 1, m_{abs} can be converted from m_{ex} via the adsorbed phase density ρ_a [4,35],

$$m_{abs} = \frac{m_{ex}}{1-\rho_b/\rho_a}. \quad (1)$$

In previous works, ρ_a was assumed to be a constant as the liquid density of methane at normal boiling point [36–38]. Still assuming constant ρ_a, some empirical approaches such as Langmuir model [39], supercritical Dubinnin-Radushkevich model [24], and Ono-Kondo lattice model [8] have been used to characterize the absolute adsorption in shale by fitting experimentally measured m_{ex} using Eq. (1). However, it is well known that adsorbed phase density is dependent on pressure and temperature [20] and varying ρ_a at different pressures from grand canonical Monte Carlo (GCMC) simulations has been used to obtain m_{abs} [26].

Another approach is to use the adsorbed phase volume V_a to get m_{abs} from m_{ex},

$$m_{abs} = m_{ex} + V_a\rho_b. \quad (2)$$

In our previous work [21], we used GCMC simulations to characterize the adsorbed phase from methane density distributions in clay nanopores. The adsorbed phase was defined as the area between the boundary obtained from the effective pore volume and the local minima between the first and second adsorption layers at high pressures. We have shown that in micropores (less than 2 nm), methane density distribution is very different from bulk and total adsorption should be regarded as the absolute adsorption. For given adsorbed phase (given ρ_a and V_a), Eq. (2) provides better estimations of absolute adsorption than Eq. (1), but still showing noticeable over-estimation due to the presence of transition zone at intermediate pressure conditions [21,40,41]. While the transition zone is excluded from the adsorbed phase, it contributes to m_{ex}, and eventually m_{abs} as depicted in Eqs. (1) and (2) [21]. Although molecular simulations can be used to explicitly characterize the transition zone, they come with expensive computational costs. Such computational burden associated with molecular simulations askes for more efficient and computationally less expensive approaches to accurately characterize the absolute adsorption, especially from experimental measurement.

Langmuir model [42] has been widely used to calculate the absolute adsorption of gas on a solid surface [43]. It is based on a monolayer adsorption of gas molecules on an ideal planar surface, describing surface coverage [44]. Thus, Langmuir model cannot describe the effect of pore size distributions and confinement in shale. Dubinnin-Radushkevich (DR) model [45,46] based on pore filling method, assuming a mean value for the force field for all adsorbate molecules in the pore [47], was used to study the gas adsorption up to the bulk saturation vapor pressure. Later, Sakurovs *et al.* [48] proposed supercritical DR (SDR) model by replacing vapor pressure by adsorbed phase density to study supercritical fluid adsorption in porous media. Although SDR has been widely used in the characterization of absolute adsorption in shale, the pore-filling model which does not differentiate the adsorbed and free gas phases is not in line with the adsorption model shown in Fig. 1. Recently, Ono-Kondo (OK) model [49–53] based on lattice theory has been used to study the absolute adsorption in shale [8]. OK model assumes that gas molecules occupy the lattice sites in chemical equilibrium with bulk and can be used to study supercritical gas adsorption in nanopores. As we will show later, for a given layer width, it can readily calculate excess adsorption without using Eqs. (1) and (2). In addition, because OK model can consider multilayer lattice structure [52], it can potentially characterize the transition zone. Previously, there have been some works using OK model with single-layer structure in nanopores [8,54–56], neglecting the fluid-fluid interactions and thus reducing to Langmuir model, which cannot take into account the transition zone.

Since slit-like pores widely exist in shale rocks [57,58], in this work, we adopt the slit pore geometry as in our previous works [20,59,60] to perform GCMC simulations to investigate methane adsorption behavior in carbon nanopores under a wide range of pressures and compare with OK model with multilayer structure. Moreover, the slit pore geometry in GCMC simulation is in line with the cubic lattice structures assumed in OK model. We perform GCMC simulation to model methane adsorption in organic materials, which are mainly kerogen that have pores in nanometer range. There have been a number of works using full atomistic models to represent kerogen [61–63]. However, the rough surfaces used in these kerogen models may not represent a fair comparison between molecular simulations and OK model. In addition, the simplified carbon slit-pore model has shown an excellent agreement with experiments on gas adsorption in shale [33]. Methane molecules are considered as single-site Lennard Jones (LJ) particles in our simulation. Excess adsorption is calculated based on the same approach as in the volumetric method, and the effective pore volume is obtained by helium adsorption. We also propose a modified adsorption model to take into account the transition zone. OK model with multilayer structure is used to fit the excess adsorption obtained from GCMC simulations to calculate the absolute adsorption in each layer. The number and width of layer in OK model are pre-determined based on the density distributions from GCMC simulations. In addition, we also compare the OK model with multilayer structure (OK-MU) with that with monolayer structure (OK-MO).

The remainder of this paper is organized as follows. In Section 2, we describe the OK lattice model. In Section 3, we introduce the molecular simulation methods and define the molecular models. In Section 4, we will first study the methane excess adsorption and density distributions in carbon nanopores from GCMC simulations. Based on the characteristics of density distributions, we propose a modified adsorption model to study the effect of transition zone and absolute adsorption. Then, we will use OK-MU to compare with GCMC simulations on the absolute adsorption as well as OK-MO. In Section 5, we summarize key conclusions and discuss potential implications.

2. Ono-Kondo lattice model

In this work, following the work by Aranovich and Donohue [52], we consider lattice theory of three-dimensional cubic geometry for a single-component adsorbate, assuming the adsorbate is in contact with a planar surface at $i = 0$. The classical equations of thermodynamic equilibria for the lattice model based on the mean-field approximation

are [51]

$$\ln\left[\frac{x_i(1-x_b)}{x_b(1-x_i)}\right] + (z_1x_{i+1} + z_2x_i + z_1x_{i-1} - z_0x_b)\frac{\varepsilon}{k_BT} = 0, \quad i \geqslant 2, \tag{3}$$

$$\ln\left[\frac{x_1(1-x_b)}{x_b(1-x_1)}\right] + (z_1x_2 + z_2x_1 - z_0x_b)\frac{\varepsilon}{k_BT} + \frac{\varepsilon_s}{k_BT} = 0, \quad i = 1. \tag{4}$$

where ε is adsorbate-adsorbate interaction energy, ε_s is adsorbate-adsorbent interaction energy, z_0 is the bulk coordination number, z_2 is the coordination number within one layer and $z_1 = (z_0 - z_2)/2$. In general, the more negative of ε and ε_s, the stronger of the fluid-fluid and fluid-surface interactions, respectively. For a cubic lattice configuration, $z_0 = 6$, $z_1 = 1$, $z_2 = 4$. x_i is the fraction of absorbed phase molecules occuping the layer i and x_b is the fraction of molecules in the bulk phase. In this work, the occupation fractions are given as,

$$x_i = \frac{\rho_{a,i}}{\rho_{am}}, \tag{5}$$

$$x_b = \frac{\rho_b}{\rho_{am}}, \tag{6}$$

where $\rho_{a,i}$ is the adsorbate density in layer i, ρ_{am} is the maximum adsorbate density in each layer and ρ_b is the bulk adsorbate density. While ρ_{am} is fixed and obtained from the fitting, the actual adsorption in each layer is dependent on the system pressure and determined by the fluid-fluid and fluid-surface interactions.

Assuming constant layer volume (width) V_a, the Gibbs (excess) adsorption amount can be given as,

$$m_{ex} = \rho_{am}V_a\sum_{i=1}^{n}(x_i - x_b). \tag{7}$$

where n is the number of layers and m_{ex} is the excess adsorption amount.

In some of previous works [8,54–56], methane adsorption is only considered as monolayer and methane-methane interaction is neglected, reducing the adsorption behavior to Langmuir isotherm. In addition, the expression of excess adsorption in Bi *et al.*'s work [8] is mistaken as the absolute adsorption, leading to a significant error in the calculated adsorption capacity [64]. Benard *et al.* [65] used two-layer adsorption model to fit methane adsorption in activated carbon CNS-201 with temperature ranging from 243 to 333 K and pressure up to 16 MPa. They used a temperature-dependent variable to represent the maximum monolayer adsorption capacity and other fitting parameters are maximum monolayer adsorbed phase density, fluid-fluid interaction and fluid-surface interaction. Sudibandriyo *et al.* [66] and Merey *et al.* [67,68] used Ono-Kondo model to fit methane adsorption isotherm with hexagonal lattice cell configuration. In their so-called two-parameter OK model, the fluid-surface interaction is regressed for specific adsorption system, while the maximum monolayer adsorption capacity is fitted by each adsorption isotherm. The constant fluid-fluid interaction is obtained from the proportional relation to the well depth of the LJ 12-6 potential and the constant maximum adsorbed phase density is estimated based on the saturated methane density under critical condition. In their regression, both of those two parameters are fixed. As a result, the adsorbed phase width is dependent on temperature and pressure. However, in previous molecular simulations [21], it has been shown that methane adsorption layer width is rather a constant close to the diameter of methane molecule.

2.1. OK-MU

In our work, OK-MU considering both adsorbate-adsorbate and adsorbate-adsorbent interactions are applied to characterize methane adsorption in nanopores. The width of adsorbed layer is fixed as the methane LJ diameter of 0.38 nm based on previous simulation works [21,40]. In the case of 4 nm pore, as we will show later, beyond two noticeable adsorption layers, methane density distribution is close to the bulk. To ensure robust and reliable fittings to the excess adsorption and accurate prediction of the absolute adsorption in adsorption layers, we use three-layer structures in OK-MU, in which beyond the third layer the density is the same as bulk. In fact, as we will show later, the density of the third layer in OK-MU is close to the bulk density. Therefore, the OK-MU is given as,

$$\begin{cases} \ln\left(\frac{x_3(1-x_b)}{x_b(1-x_3)}\right) + (4x_3 + x_2 - 5x_b)\frac{\varepsilon}{k_BT} = 0 \\ \ln\left(\frac{x_2(1-x_b)}{x_b(1-x_2)}\right) + (4x_2 + x_1 + x_3 - 6x_b)\frac{\varepsilon}{k_BT} = 0 \\ \ln\left(\frac{x_1(1-x_b)}{x_b(1-x_1)}\right) + (4x_1 + x_2 - 6x_b)\frac{\varepsilon}{k_BT} + \frac{\varepsilon_s}{k_BT} = 0 \end{cases}. \tag{8}$$

Eq. (8) is a set of non-linear equations which can be solved iteratively.

2.2. OK-MO

For comparison, the OK-MO considering adsorbate-adsorbate and adsorbate-adsorbent interactions can be expressed as,

$$\ln\left(\frac{x_1(1-x_b)}{x_b(1-x_1)}\right) + (4x_1 - 5x_b)\frac{\varepsilon}{k_BT} + \frac{\varepsilon_s}{k_BT} = 0. \tag{9}$$

By combining Eqs. (7) and (8) for OK-MU and Eqs. (7) and (9) for OK-MO, we fit the excess adsorption from OK models to that from GCMC simulations with fitting parameters ρ_{am}, ε and ε_s. We use sequential quadratic programming (SQP) optimization method implemented in MATLAB to obtain those three parameters.

3. Molecular model and simulation

In this work, we carry out GCMC simulations to model methane adsorption behavior in carbon nanopores. Graphite slabs are used to represent pore surface walls which havs dimensions of 6 nm × 6 nm in $x-y$ plane parallel to the pore surface with two-dimensional periodic boundary conditions. The pore width W is characterized by the separation of two rigid planar structureless carbon surfaces in z direction. The results from 6 nm by 6 nm dimensions in x-y plane can replicate that with larger dimensions (i.e., 8 nm by 8 nm).

In our simulation, we use a single site model to describe methane and helium molecules. The TraPPE force field is used to represent the methane intermolecular interactions [69]. Intermolecular interactions are represented by pairwise-additive LJ 12-6 potentials,

$$u_{LJ}(r) = 4\varepsilon_f\left[\left(\frac{\sigma_f}{r}\right)^{12} - \left(\frac{\sigma_f}{r}\right)^{6}\right], \tag{10}$$

where r is the separation distance; $\sigma_f = 0.373$ nm and $\varepsilon_f/k_B = 148.0$ K are size and energy parameter for methane [69], respectively; $\sigma_f = 0.264$ nm and $\varepsilon_f/k_B = 10.9$ K are size and energy parameter for helium [70], respectively.

In this work, pores are of slit geometry with smooth and structureless carbon surfaces. We use the 10-4-3 Steele potential to describe the fluid-wall interaction φ_{wf} [71],

$$\varphi_{wf}(z) = 2\pi\rho_w\varepsilon_{wf}\sigma_{wf}^2\Delta\left[\frac{2}{5}\left(\frac{\sigma_{wf}}{z}\right)^{10} - \left(\frac{\sigma_{wf}}{z}\right)^{4} - \frac{\sigma_{wf}^4}{3\Delta(0.61\Delta + z)^3}\right], \tag{11}$$

where $\rho_w = 114\ \text{nm}^{-3}$, $\varepsilon_{wf} = \sqrt{\varepsilon_w\varepsilon_f}$ with $\varepsilon_w = 28$ K, $\sigma_{wf} = (\sigma_w + \sigma_f)/2$ with $\sigma_w = 0.3345$ nm, and $\Delta = 0.335$ nm, respectively. The external potential Ψ in a slit pore is expressed as

$$\Psi(z) = \varphi_{wf}(z) + \varphi_{wf}(W - z), \tag{12}$$

where W is the slit-pore size.

The GCMC simulation is carried out under grand canonical (μVT) ensemble. In each MC cycle, a trial random displacement is applied to a

randomly selected gas molecule and a gas molecule is randomly removed from or inserted into the simulation box at equal probability depending on the chemical potential of gas. The chemical potentials of methane and helium molecules at given pressure and temperature conditions are obtained from the Widom insertion method [72] in canonical (*NVT*) ensemble in bulk. The bulk densities are from the National Institute of Standards and Technology (NIST) Chemistry Webbook. MC moves are implemented by the Metropolis algorithm [73]. We conduct 0.5 million MC cycles per methane molecules for equilibration and 2 million MC cycles per methane molecules for sampling density distributions. We found that doubling MC cycles (one million for equilibration and 4 million for sampling) yields the same results.

The effective pore volume is necessary for the excess adsorption calculation in volumetric method. Helium adsorption is generally used to measure the effective pore volume assuming that helium fills the pore space instead of adsorbed on the surface [13,18]. We use total helium uptake at various pressures and constant temperature to calculate effective pore volume similar to experiment [18],

$$V_p = \frac{\langle N_{He} \rangle}{N_A \rho^m_{He,b}}, \tag{13}$$

where V_p is the effective pore volume, $\langle N_{He} \rangle$ is the ensemble averaged total number of helium molecules, N_A is the Avogadro constant and $\rho^m_{He,b}$ is the molar density of bulk helium. As in our previous work [21], we obtain helium adsorption at 5 pressure points of 2, 4, 6, 8 and 10 MPa and 333.15 K. The effective pore volume is obtained as the average of volumes from those conditions. In our work, the calculated effective pore width for 4 nm and 8 nm nanopores are 3.84 nm and 7.84 nm, respectively. The reduction of 0.16 nm is due to the finite size (excluded volume) effect of helium molecules [74]. In GCMC simulation, the effective pore volume obtained by helium adsorption would affect the excess adsorption. At given pressure and temperature conditions, the excess adsorption is a linear function of the effective pore volume (width). We found that helium does show adsorption on the carbon surfaces as shown in Fig. B-1, which is different from our previous work for clay minerals [21]. Such helium adsorption on the surface can lead to an overestimation of the effective pore width.

4. Results and discussion

In this section, we will first study the methane excess adsorption and density distributions in carbon nanopores from GCMC simulations. Based on the characteristics of density distributions, we propose a modified adsorption model to study the effect of transition zone and absolute adsorption. Then, we will use OK-MU to compare with GCMC simulations as well as OK-MO on the absolute adsorption.

4.1. Methane adsorption behavior from GCMC simulation

4.1.1. Excess adsorption and density profiles

In our GCMC simulation, excess adsorption is obtained based on the volumetric method [21],

$$m_{ex} = \frac{\langle N_{C_1} \rangle / N_A - V_p \rho^m_{C_1,b}}{2 S_A}, \tag{14}$$

where $\langle N_{C_1} \rangle$ is the ensemble averaged number of methane molecules at given temperature and pressure in the nanopores, $\rho^m_{C_1,b}$ is the molar density of methane in the bulk at given conditions and S_A is the specific surface area of the pore. In this work, we use mmol/m^2 to describe the excess adsorption amount.

Fig. 2 shows the methane excess adsorption from GCMC simulation in nanopores of 4 nm and 8 nm at 333.15 K and pressures up to 50 MPa. The excess adsorption first increases to a maximum around 15 MPa, then decreases with pressure. When pressure is relatively low, methane molecules tend to adsorb on the surface and the bulk density is much lower than the adsorbed phase density. As pressure increases, the adsorbed phases may have been readily filled, while methane molecules accumulate in the bulk phase. Thus, as pressure further increases, excess adsorption decreases. Additionally, despite some GCMC simulations stated that the excess adsorption decreases with increasing pore width even in mesopores [75,76], we observe that the excess adsorption is independent to the pore width when $W \geqslant 4$ nm as reported by Chen *et al.* [77] and Tian *et al.* [21].

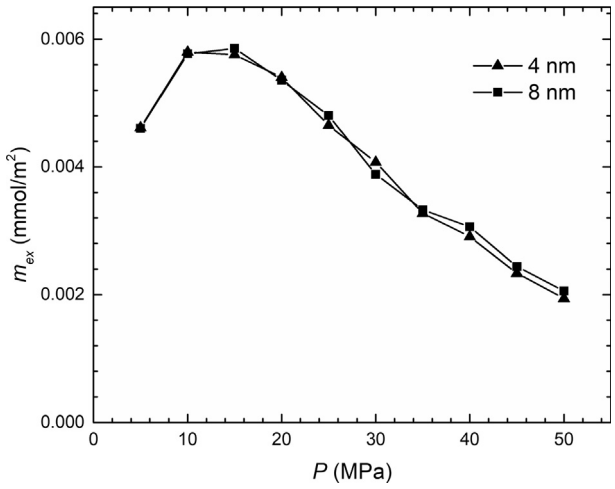

Fig. 2. Excess adsorption amount per specific surface area from GCMC simulation in carbon nanopores of various sizes at 333.15 K.

To better understand adsorption behavior, we present the methane density distributions in carbon nanopores of $W = 4$ nm and $W = 8$ nm at various pressures and 333.15 K in Fig. 3. Methane forms a strong surface adsorption and density in the middle of the pores reaches bulk. Beyond the strong first adsorption layer, a second adsorption layer can be seen in line with other simulation works [21,41,75,78]. The distance between the peaks of first and second adsorption layers is close to the methane LJ molecular size. Similar to our previous work [21], the positions of peak and local minima in density distributions at high pressures remain the same. Such second adsorption layer can be considered as transition zone. While transition zone is obvious at relatively low pressures (for example, 10 MPa), it becomes less significant at high pressures. The presence of transition zone contributes to the excess adsorption, and thus, negatively impacts the accuracy of absolute adsorption from Eqs. (1) and (2). In our previous work [21], we also observed the second adsorption layer in methane adsorption in various clay nanopores, which can be “averaged out” in the free gas zone. However, due to stronger fluid-surface interactions in carbon nanopores than that in clay nanopores, the second adsorption layer in this work is more significant. Therefore, we need to explicitly characterize the second adsorption layer in carbon nanopores. At high pressure conditions, beyond the second adsorption layer, a weak third adsorption layer can be observed. However, the average density deviation from bulk in the third adsorption layer is much smaller than that in the first and second adsorption layers.

4.1.2. Characterization of methane adsorption model

Fig. 4 exhibits the schematic representation of the first and second adsorbed layer in carbon nanopores based on GCMC simulation. The region $z_{AA'}$ defines the effective pore volume (width), which is obtained by $z_{AA'} = V_p/S_A$. The modified adsorption model can be separated into three distinct parts: the first adsorption layer, the second adsorption layer (transition zone) and free gas zone. The third adsorption layer observed in Fig. 3 is lumped into the free gas zone. The first adsorbed layer is defined as the zone between point A and point B, which is the local minima of the density profile between the first and second layer. The second adsorbed layer is defined as the region between point B and

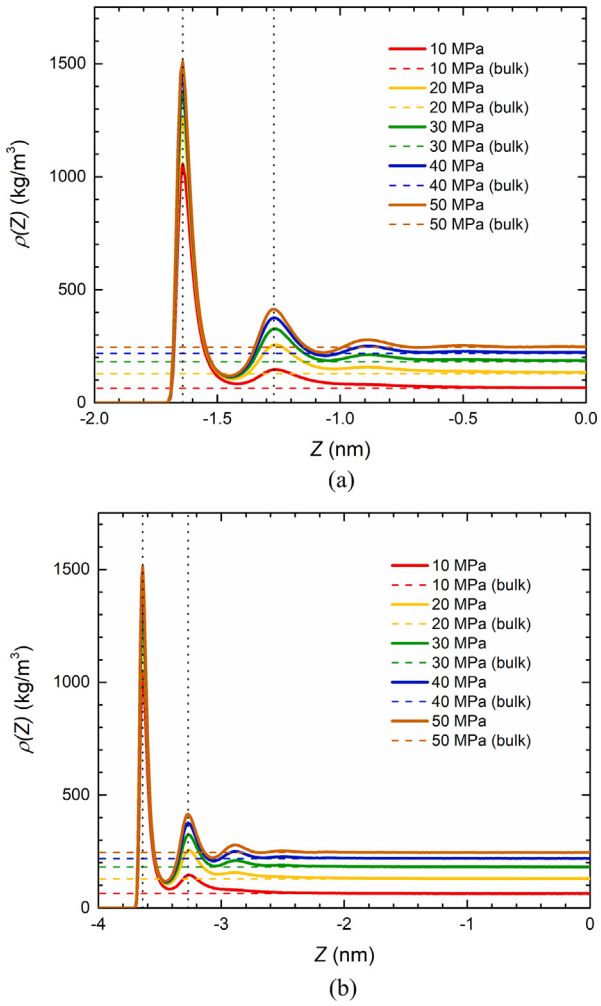

Fig. 3. Methane density distributions from GCMC simulation at 333.15 K and various pressures in carbon nanopores of (a) $W = 4$ nm; (b) $W = 8$ nm. For comparison, the bulk densities from NIST Chemistry Webbook are depicted as dashed lines. The dotted lines represent the peaks in the density profiles.

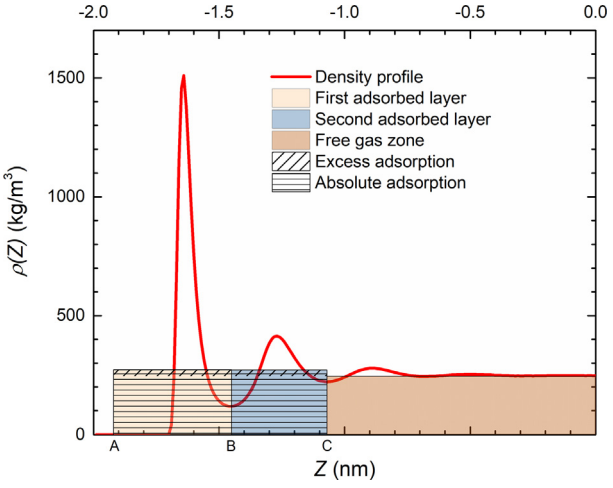

Fig. 4. Schematic representation of the first and second adsorbed layer in carbon nanopore of $W = 4$ nm based on GCMC simulation at 333.15 K and 50 MPa. The heights of adsorbed phase density of the first adsorbed layer, second adsorbed layer and free gas zone are obtained by $\rho_{a1} = \int_A^B \rho(z)dz/z_{AB}$, $\rho_{a2} = \int_B^C \rho(z)dz/z_{BC}$, and $\rho_f = \int_C^{C'} \rho(z)dz/z_{CC'}$, respectively.

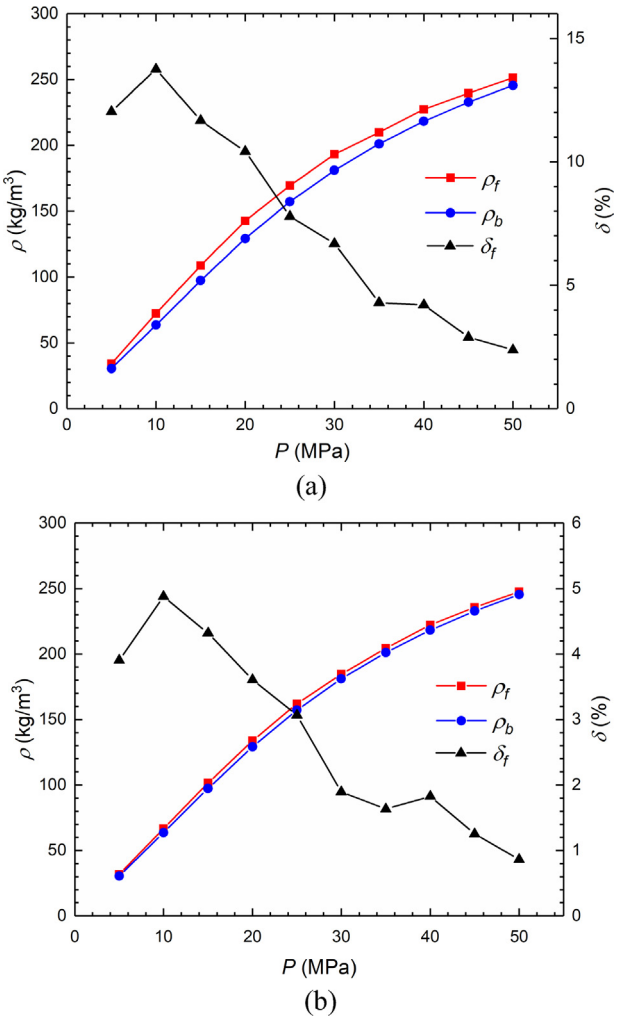

Fig. 5. Comparison of free gas density from GCMC simulation and bulk density from NIST Chemistry Webbook and their relative error $\delta_f = (\rho_f - \rho_b)/\rho_b$ in carbon nanopores of (a) $W = 4$ nm; (b) $W = 8$ nm at 333.15 K.

point C, which is the local minima of the density profile between the second layer and free gas zone. The point B and point C are defined from the density distributions at 50 MPa. A number of simulation works revealed that the width of adsorbed phase should equal to the diameter of LJ molecules [21,40,41,75,79]. In our work, we observe that the width of AB, $z_{AB} = 0.47$ nm is larger than the methane LJ diameter of 0.38 nm, because helium can form adsorption layer on carbon surfaces which in turn increases the effective pore volume. On the other hand, the width of BC is 0.38 nm. The region between C and C' is defined as the free gas zone. In Fig. 4, the heights of the first adsorbed layer, second adsorbed layer and free gas zone are defined as $\rho_{a1} = \int_A^B \rho(z)dz/z_{AB}$, $\rho_{a2} = \int_B^C \rho(z)dz/z_{BC}$ and $\rho_f = \int_C^{C'} \rho(z)dz/z_{CC'}$, respectively.

In order to calibrate our modified adsorption model, we depict the density of free gas zone from GCMC simulation comparing to the bulk density from NIST Chemistry Webbook in Fig. 5. For clarity, we also present their relative errors $\delta_f = (\rho_f - \rho_b)/\rho_b$. At higher pressures up to 50 MPa, the relative errors are less than 3% for $W = 4$ nm and less than 1% for $W = 8$ nm. At low pressures, the variation between ρ_f and ρ_b can be around 14% at 10 MPa in 4 nm pores, due to strong fluid-surface interactions. Despite the relatively large difference between ρ_f and ρ_b at intermediate pressures, ρ_f approaches ρ_b as pressure increases.

In Fig. 6, we present the adsorbed phase densities in each adsorbed layer obtained by GCMC simulation and the relative difference

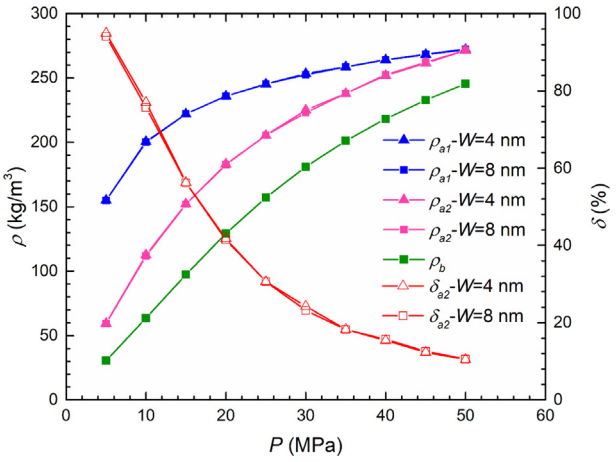

Fig. 6. Adsorbed phase density in each adsorbed layer from GCMC simulation and bulk density from NIST Chemistry Webbook. We also present the relative difference $\delta_{a2} = (\rho_{a2}-\rho_b)/\rho_b$ in second layer in carbon nanopore of $W = 4$ nm and $W = 8$ nm at 333.15 K.

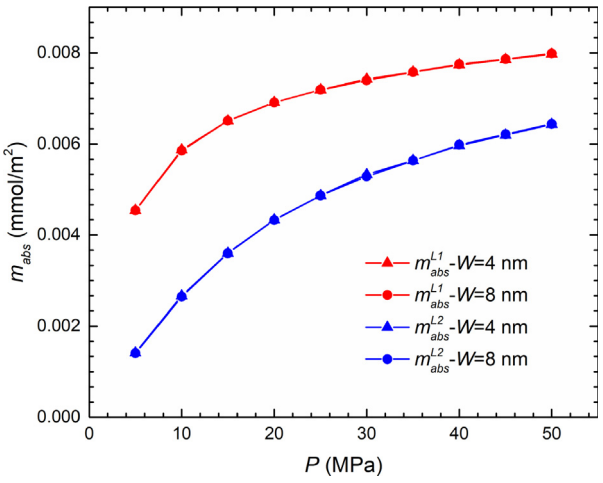

Fig. 7. Absolute adsorption amount per specific surface area of the first and second adsorbed layer in carbon nanopores of $W = 4$ nm and $W = 8$ nm at 333.15 K from GCMC simulation.

$\delta_{a2} = (\rho_{a2}-\rho_b)/\rho_b$ in carbon nanopores of $W = 4$ nm and $W = 8$ nm at 333.15 K. Both ρ_{a1} and ρ_{a2} increase continuously with pressure. It is noted that ρ_{a2} is significantly higher than ρ_b. At high pressures (50 MPa), the discrepancy between ρ_{a2} and ρ_b is around 10%; while, at low pressures, δ_{a2} can be as high as 95%, indicating the strong effect of transition zone. It is necessary to explicitly consider the second adsorption layer, which is different from the free gas and contribute to the excess adsorption calculation. In our previous work [21], the methane second adsorption layer in clay nanopores can be "averaged out" in the free gas zone. It is because fluid-surface interactions in clay nanopores are weaker than that in carbon nanopores.

Based on the modified adsorption model as shown in Fig. 4, the absolute adsorption can be divided by two parts:

$$m_{abs} = m_{abs}^{L1} + m_{abs}^{L2}, \tag{15}$$

where

$$\begin{cases} m_{abs}^{L1} = \rho_{a1} V_{a1} \\ m_{abs}^{L2} = \rho_{a2} V_{a2} \end{cases}, \tag{16}$$

$$\begin{cases} V_{a1} = 2 S_A z_{AB} \\ V_{a2} = 2 S_A z_{BC} \end{cases}, \tag{17}$$

in which, m_{abs} is the total adsorption amount in layer one and two, m_{abs}^{L1} and m_{abs}^{L2} represent the absolute adsorption amount in the first layer and second layer, respectively, V_{a1} and V_{a2} are the first and second adsorbed phase volume, respectively. In Fig. 7, we present the calculated absolute adsorption amount per specific surface area of the first and second adsorbed layer in carbon nanopores of $W = 4$ nm and $W = 8$ nm at 333.15 K from GCMC simulation. The absolute adsorption amount increases continuously with pressure up to 50 MPa for both layers. As shown in Fig. 6, because the density distributions near the surface are similar when $W \geqslant 4$ nm, the absolute adsorption remains the same.

4.2. Adsorption behavior from OK-MU

In this section, we assess the OK-MU by comparing to GCMC simulations and OK-MO. Since the methane density distribution in slit-pore is symmetric and excess adsorption amount is expressed as per specific surface area, we only simulate methane adsorption on one carbon surface assuming three-layer structures. We fit the excess adsorption with constant layer width of $z_{OK} = 0.38$ nm for methane adsorption isotherm in carbon nanopore of $W = 4$ nm at 333.15 K as shown in Fig. 8. The three fitting parameters have fitting ranges as :

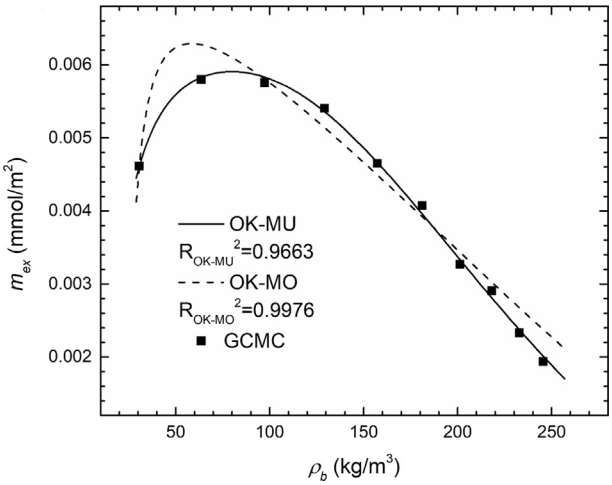

Fig. 8. OK-MU and OK-MO with constant layer width of 0.38 nm for fitting methane excess adsorption from GCMC simulation in carbon nanopore of $W = 4$ nm at 333.15 K.

$0 < \rho_{am} < 700$ kg/m^3, $-1 < \varepsilon/k_BT < 0$ and $-10 < \varepsilon_s/k_BT < 0$ [50–53]. The calculated fitting parameters are $\rho_{am} = 335.32$ kg/m^3, $\varepsilon/k_BT = -0.49$ and $\varepsilon_s/k_BT = -1.82$ with R-square of $R^2 = 0.9976$ for OK-MU; $\rho_{am} = 390.82$ kg/m^3, $\varepsilon/k_BT = -0.83$ and $\varepsilon_s/k_BT = -1.19$ with R-square of $R^2 = 0.9663$ for OK-MO. To be noted that in actual experimental measurements, these fitting parameters may vary from different experimental conditions and samples.

Overall, while OK-MU shows an excellent agreement with GCMC simulation, OK-MO presents some discrepancies. There have been a number of works using a constant adsorbed phase density as 424 kg (the liquid methane density at its boiling point of 112 K and 0.1 MPa) or 373 kg/m^3 (the saturated methane density at critical point, 190.56 K and 4.58 MPa) [8,80,81]. In addition, assuming a constant adsorbed phase density which is independent of pressure, it can also be obtained by fitting the measured excess adsorption with models such as Langmuir, SDR and OK [8,23,24,39,54]. Do *et al.* [82] claimed that the adsorbed phase density could be very close to the liquid methane density at high pressure, but would not be equal or higher than that. Tian *et al.* [24] used both Langmuir and SDR models to fit experimental excess adsorption data. They found that the adsorbed phase density fitted by Langmuir model would exceed liquid methane density, while that from SDR model is generally smaller than 424 kg/m^3, ranging from

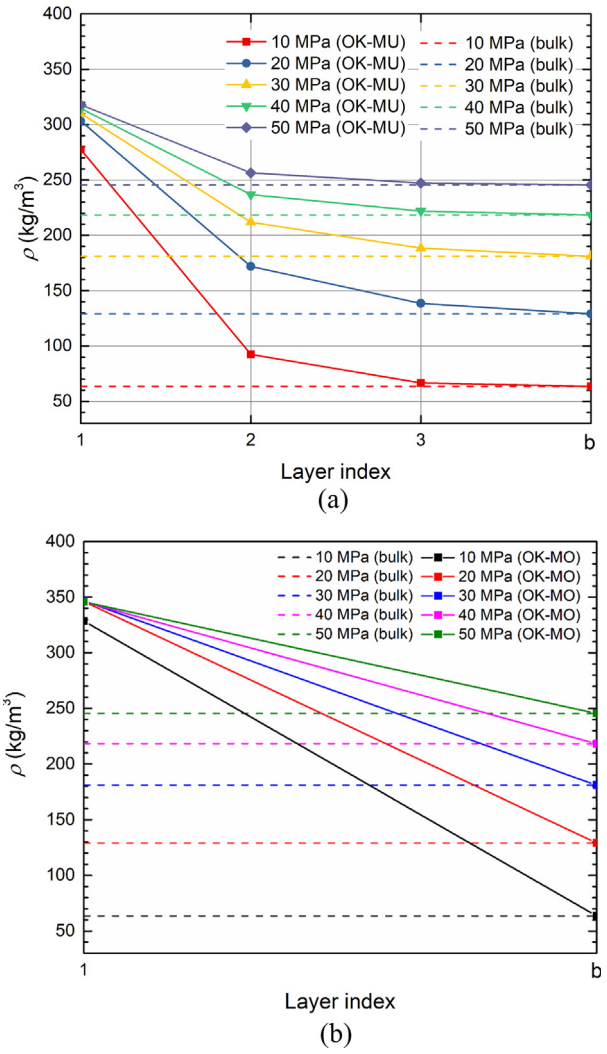

Fig. 9. Densities of each layer from (a) OK-MU; (b) OK-MO in carbon nanopores of $W = 4$ nm at 333.15 K.

297 kg/m^3 to 415 kg/m^3. Bi *et al.* [8] found that by using OK model regression, the free fitting result of maximum adsorbed phase density is unreasonable (higher than 424 kg/m^3). Thus, they fixed the adsorbed phase density as a constant value of 373 kg/m^3. In the work by Sudibandriyo *et al.* [66], the regressed methane adsorbed phase density on dry activated carbons from OK model is 345 kg/m^3. In our work, the maximum adsorbed phase density from OK-MU is lower than liquid methane density.

Fig. 9(a) presents the corresponding densities of each layer from OK-MU at various pressures. The densities of the first and second layer are significantly higher than ρ_b, while the density of the third layer is close to ρ_b. We also plot the calculated densities in OK-MO for comparison in Fig. 9(b). The adsorption layer densities are much higher than bulk densities and become readily saturated as pressure increases. In Fig. 10, we present the absolute adsorption amount per specific surface area in the first and second layer from OK-MU and GCMC as well as the first layer from OK-MO, and their relative differences $\delta = (m_{abs-GCMC} - m_{abs-OK})/m_{abs-GCMC}$. For OK-MU, the calculated absolute adsorption of the first and second layers are expressed as $m^{L1}_{abs,OK} = \rho_{a1,OK} z_{OK}$ and $m^{L2}_{abs,OK} = \rho_{a2,OK} z_{OK}$, respectively. Overall, the agreement between OK-MU and GCMC simulation is very good. It can be seen from Fig. 10(a) that when only monolayer is considered in OK model, the calculated absolute adsorption amount is always overestimated comparing to GCMC simulation and maximum δ is around −33%. As shown in Fig. 10(b), the absolute adsorption obtained by OK-

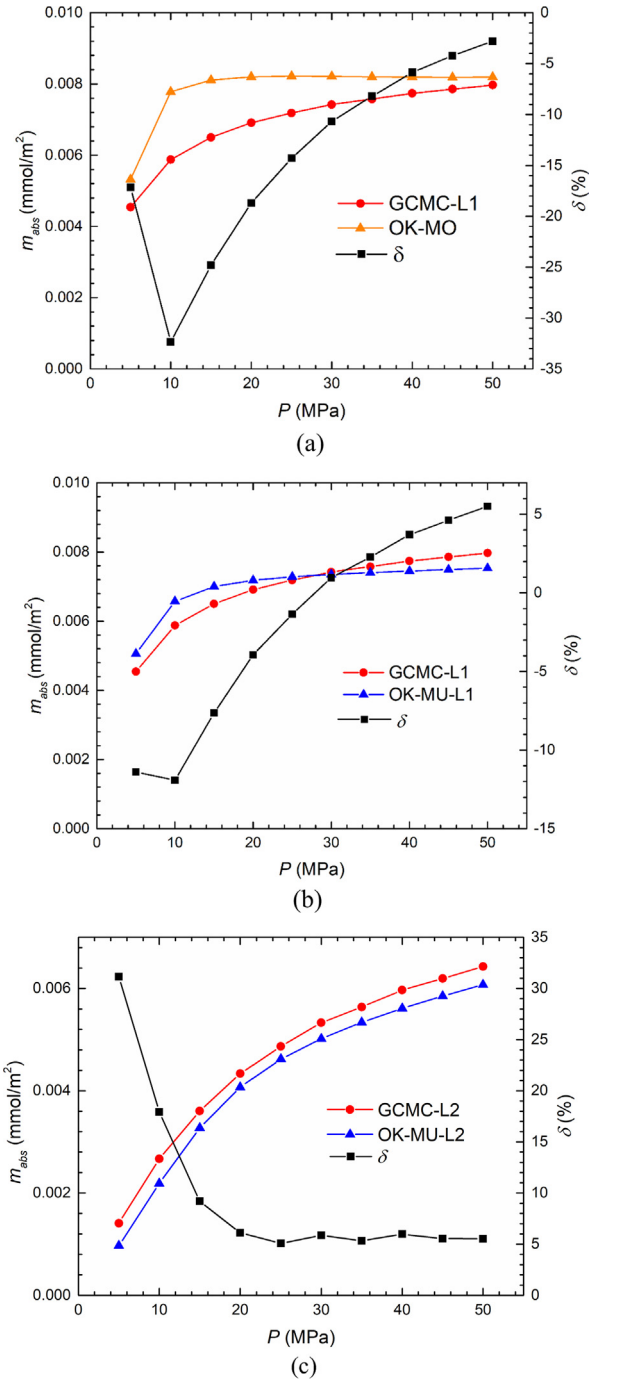

Fig. 10. Absolute adsorption amount per specific surface area from GCMC simulation, OK-MU, OK-MO and relative differences $\delta = (m_{abs-GCMC} - m_{abs-OK})/m_{abs-GCMC}$ of $W = 4$ nm at 333.15 K. (a) The first layer from OK-MO; (b) The first layer from OK-MU; (c) The second layer from OK-MU.

MU is firstly higher than that obtained by GCMC simulation and then underestimates the absolute adsorption from 30 MPa, while maximum δ is around −13%. As shown in Fig. 10(c), the second layer absolute adsorption from OK-MU is underestimated over given pressure range and δ decreases with pressure, around 5% at pressure up to 50 MPa.

We present the combined methane absolute adsorption amount in the first and second layers from OK-MU and GCMC simulation in Fig. 11. The maximum relative deviation $\delta = (m_{abs-GCMC} - m_{abs-OK})/m_{abs-GCMC}$ is less than 6%, indicating an excellent agreement between OK-MU model and GCMC simulation.

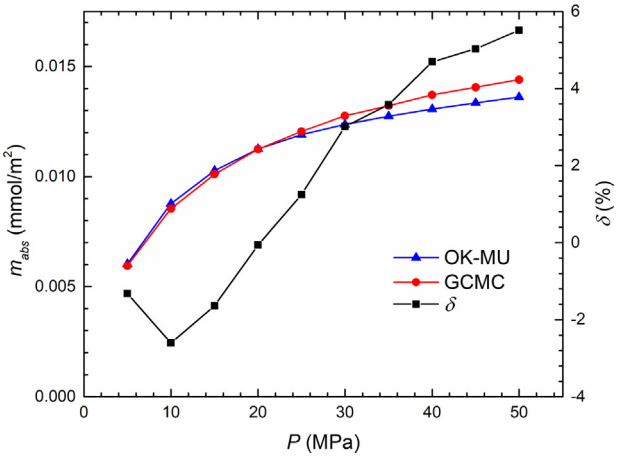

Fig. 11. Comparison of combined absolute adsorption amount per specific surface area obtained by OK-MU and GCMC simulation and their relative error $\delta = (m_{abs-GCMC} - m_{abs-OK})/m_{abs-GCMC}$ in carbon nanopore of $W = 4$ nm at 333.15 K.

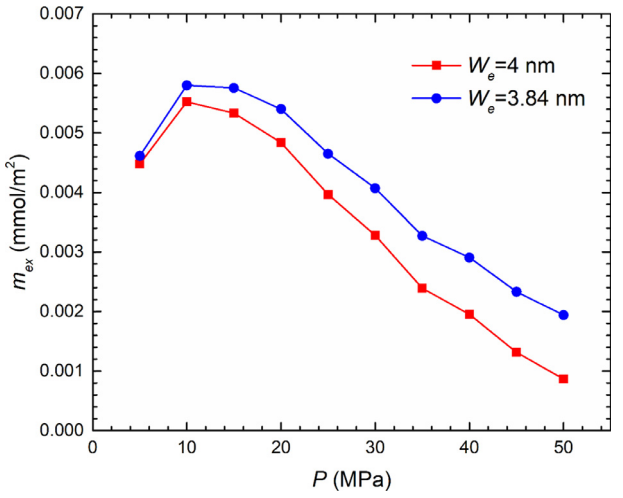

Fig. 12. Comparison of excess adsorption amount per specific surface area with different effective pore widths W_e in carbon nanopores at 333.15 K.

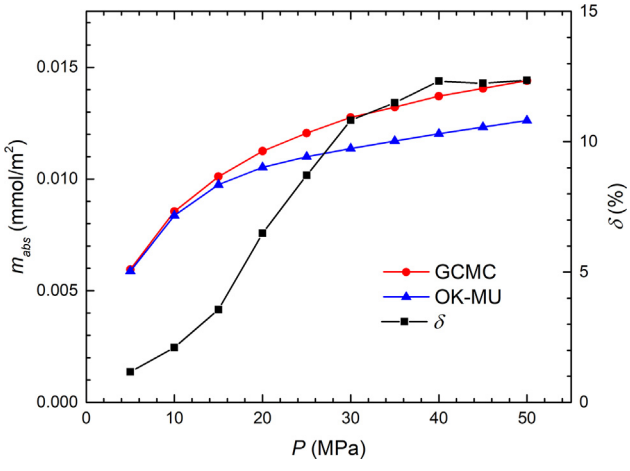

Fig. 13. Comparison of combined absolute adsorption amount per specific surface area and their relative error $\delta = (m_{abs-GCMC} - m_{abs-OK})/m_{abs-GCMC}$ from GCMC simulation and OK-MU in carbon nanopore of $W_e = 4$ nm at 333.15 K.

In addition, the excess adsorption is sensitive to the effective pore volume [74]. Do and his coworkers mentioned that the effective pore volume would significantly affect the excess adsorption [83]. Moreover, the effective pore volume of the sample cannot be directly measured in the gravimetric method. Thus, in this work, we arbitrarily change the effective pore volume to test the performance of OK-MU. We plot the excess adsorption assuming effective pore width of 4 nm for $W = 4$ nm pores and that with actual effective pore width of 3.84 nm in Fig. 12. Even for arbitrarily chosen pore volume, OK-MU shows a good agreement with GCMC simulation for combined absolute adsorption as shown in Fig. 13. It is shown that the maximum relative error is less than 13%.

5. Conclusion

In this work, we performed GCMC simulation to investigate the methane adsorption in carbon nanopores at various pressures. We used the volumetric method to calculate the excess adsorption, using helium adsorption to determine the effective pore volume. Based on the density distributions, we proposed a modified adsorption model for methane to better take into account the effect of transition zone.

Our simulation results showed that the excess adsorption per specific surface area is insensitive to the pore size, when $W \geqslant 4$ nm. The second adsorption layer is observed and the density can be very different from the bulk, indicating the transition zone. Such transition zone can negatively affect the accuracy of the absolute adsorption calculation based on the monolayer adsorption model as shown in Fig. 1. By using a modified adsorption model, the transition zone can be readily taken into account. OK-MU have shown an excellent agreement with GCMC simulations on the excess adsorption and accurately characterize the transition zone. We found that the absolute adsorption calculated by OK-MU yields a good agreement with GCMC simulation, and the maximum relative error between these two methods is less than 6%. In addition, we used the arbitrary effective pore width to test OK-MU. Even though a significant change in excess adsorption occurs, the OK-MU can still predict the methane absolute adsorption witha reasonable agreement with GCMC simulations. In contrast to OK-MU, the prediction from OK-MO shows noticeable discrepancies from GCMC simulations. By using the modified adsorption model and OK-MU, the methane adsorption behavior in carbon nanopores can be readily characterized. Our work should provide important insights into the accurate estimation of methane absolute adsorption, especially in experimental applications.

Although a good agreement of methane adsorption can be found between OK-MU and GCMC simulation, the limitations of our work still exist. Our newly proposed adsorption model is only applicable when $W \geqslant 4$ nm. However, it is well known that shale has extensive amount of micropores ($W \leqslant 2$ nm). Jin [84] reported that the adsorption behavior in micropores can be different from the adsorption model shown in Fig. 4. We have been conducting a separate work to take into account the effect of pore size distribution (PSD) in OK-MU to accurately and efficiently characterize the methane adsorption behavior in shale porous media.

Acknowledgement

This research was enabled in part by support provided by Westgrid (www.westgrid.ca) and Compute Canada (www.computecanada.ca). The authors also greatly acknowledge a Discovery Grant from Natural Sciences and Engineering Research Council of Canada (NSERC RGPIN-2017-05080). As a part of the University of Alberta's Future Energy Systems research initiative, this research was made possible in part thanks to funding from the Canada First Research Excellence Fund.

Appendix A. Derivation of Ono-Kondo model

Consider taking an adsorbate molecule at site k and moving it to an empty site infinitely distant, the exchange of the molecules in the lattice with a vacancy can be written as

$$M_k + V_\infty \rightarrow V_k + M_\infty \tag{A-1}$$

where M represents adsorbate molecule, V is the vacancy, k denotes the adsorbed site and ∞ is the site at infinite distance which can be seen as bulk.

If such exchange of molecules reaches equilibrium at isothermal and isobaric condition,

$$\Delta G_i = \Delta H_i - T\Delta S_i = 0, \tag{A-2}$$

where ΔG_i, ΔH_i and ΔS_i are the Gibbs free energy, enthalpy and entropy changes in each layer due to molecule exchange and T is the absolute temperature. The entropy change can be written as [52],

$$\Delta S_i = k_B \ln W_{1,i} - k_B \ln W_{2,i}, \tag{A-3}$$

$$\frac{W_{1,i}}{W_0} = x_i(1-x_b), \tag{A-4}$$

$$\frac{W_{2,i}}{W_0} = x_b(1-x_i), \tag{A-5}$$

where k_B is Boltzmann's constant, $W_{1,i}$ refers to the number of configurations where the fluid molecule occupies the absorbed phase and the site in the bulk phase is at vacancy at layer i, $W_{2,i}$ is the number of configurations where the absorbed phase is empty and fluid molecule occupies bulk phase at layer i, W_0 refers to the overall number of system configurations, x_i is the fraction of absorbed phase molecules occupies the layer i and x_b is the fraction of molecules in the bulk phase. In this work, the occupation fractions are given as,

$$x_i = \frac{\rho_{a,i}}{\rho_{am}}, \tag{A-6}$$

$$x_b = \frac{\rho_b}{\rho_{am}}, \tag{A-7}$$

where $\rho_{a,i}$ is the density of layer i, ρ_{am} is the maximum adsorbed density in each layer and ρ_b is the bulk density.

By substituting Eqs. (6) and (7) into Eq. (5), we can obtain

$$\Delta S_i = k_B \left[\frac{x_i(1-x_b)}{x_b(1-x_i)} \right]. \tag{A-8}$$

The enthalpy change for three dimensional OK model can be represented by the interactions of neighboring molecules located in the same and adjacent layers based on the mean-field approximation [52],

$$\Delta H_i = -\varepsilon(z_1 x_{i+1} + z_2 x_i + z_1 x_{i-1} - z_0 x_b), \quad i \geqslant 2, \tag{A-9}$$

where ε is adsorbate-adsorbate interaction energy, z_0 is the bulk coordination number, z_2 is the coordination number within one layer and $z_1 = (z_0 - z_2)/2$. For a cubic lattice configuration, $z_0 = 6$, $z_1 = 1$, $z_2 = 4$. Considering the interactions between adsorbate and adsorbent surface, ε_s, we have the enthalpy change when adsorbate is in the first layer:

$$\Delta H_i = -\varepsilon(z_1 x_{i+1} + z_2 x_i - z_0 x_b) - \varepsilon_s, \quad i = 1, \tag{A-10}$$

Appendix B. Helium adsorption in carbon materials

Helium adsorption is applied to obtain the effective pore width in carbon nanopores at 333.15 K. Fig. (B-1) shows the density profile of helium in 4 nm pores at various pressures. It can be seen from the figure that the helium shows an adsorption behavior near the surface, resulting in a larger

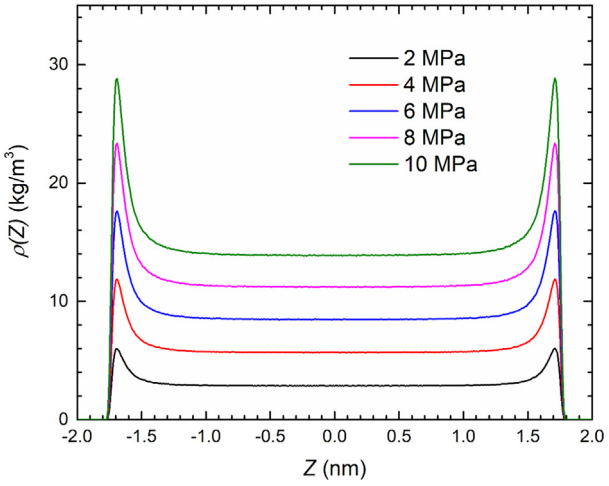

Fig. B-1. Density profiles of Helium in carbon nanopore of W = 4 nm at 333.15 K.

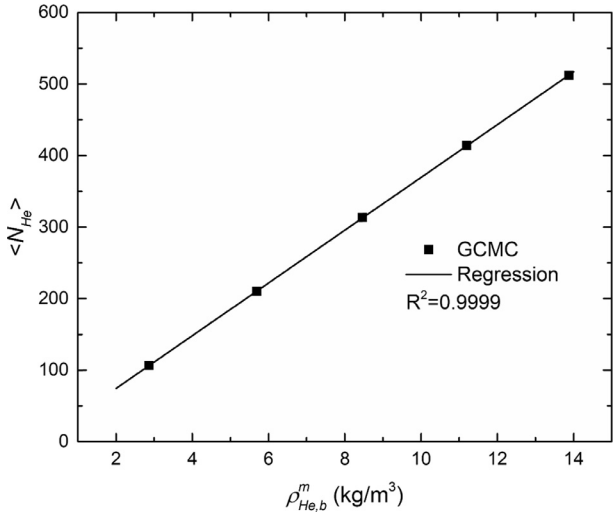

Fig. B-2. Relationship between total helium uptake and bulk density in carbon nanopore of $W = 4$ nm at 333.15 K. The symbols are from GCMC simulations and the solid line is from linear fitting.

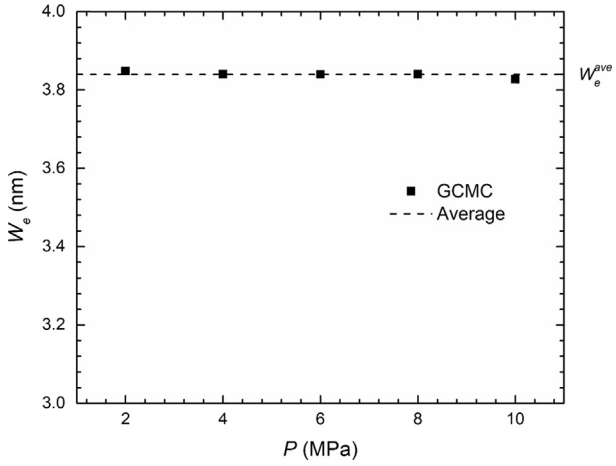

Fig. B-3. Effective pore width by helium adsorption at different pressures in carbon nanopore of $W = 4$ nm at 333.15 K. The symbols are from GCMC and the dashed line depicts the averaged pore width obtained from five pressure conditions.

effective pore width compared with our previous work [21] in clay minerals. As the same procedure of calculating effective pore width in our earlier studies, a linear relationship between $\langle N_{He} \rangle$ and $\rho^m_{He,b}$ is shown in Fig. (B-2). Thus, the calculated effective pore widths at each pressure are depicted in Fig. (B-3) using the Eq. (13). The calculated effective pore width is smaller than 4 nm, because of the finite size of helium [74].

References

[1] Curtis JB. Fractured shale-gas systems. AAPG Bull 2002;86(11):1921–38.
[2] Jarvie DM, et al. Unconventional shale-gas systems: the Mississippian Barnett Shale of north-central Texas as one model for thermogenic shale-gas assessment. AAPG Bull 2007;91(4):475–99.
[3] Montgomery SL, et al. Mississippian Barnett Shale, Fort Worth basin, north-central Texas: gas-shale play with multi–trillion cubic foot potential. AAPG Bull 2005;89(2):155–75.
[4] Rexer TF, et al. Methane adsorption on shale under simulated geological temperature and pressure conditions. Energy Fuels 2013;27(6):3099–109.
[5] Jin Z, Firoozabadi A. Thermodynamic modeling of phase behavior in Shale Media. SPE J 2016;21(1):190–207.
[6] Ross DJ, Bustin RM. The importance of shale composition and pore structure upon gas storage potential of shale gas reservoirs. Mar Pet Geol 2009;26(6):916–27.
[7] Chalmers GR, Bustin RM. Lower Cretaceous gas shales in northeastern British Columbia, Part I: geological controls on methane sorption capacity. Bull Can Petrol Geol 2008;56(1):1–21.
[8] Bi H, et al. Ono-Kondo model for supercritical shale gas storage: a case study of Silurian Longmaxi shale in southeast Chongqing China. Energy Fuels 2017;31(3):2755–64.
[9] Ross DJ, Bustin RM. Shale gas potential of the lower jurassic gordondale member, northeastern British Columbia Canada. Bull Can Petrol Geol 2007;55(1):51–75.
[10] Chalmers GR, Bustin RM. The organic matter distribution and methane capacity of the Lower Cretaceous strata of Northeastern British Columbia Canada. Int J Coal Geol 2007;70(1–3):223–39.
[11] Ross DJ, Bustin RM. Characterizing the shale gas resource potential of Devonian-Mississippian strata in the Western Canada sedimentary basin: Application of an integrated formation evaluation. AAPG Bull 2008;92(1):87–125.
[12] Strapoc D, et al. Geochemical constraints on the origin and volume of gas in the New Albany Shale (Devonian–Mississippian), eastern Illinois Basin. AAPG Bull 2010;94(11):1713–40.
[13] Zhang T, et al. Effect of organic-matter type and thermal maturity on methane adsorption in shale-gas systems. Org Geochem 2012;47:120–31.
[14] Gasparik M, et al. Geological controls on the methane storage capacity in organic-rich shales. Int J Coal Geol 2014;123:34–51.
[15] Hao F, Zou H, Lu Y. Mechanisms of shale gas storage: implications for shale gas exploration in ChinaMechanisms of Shale Gas Storage. AAPG Bull 2013;97(8):1325–46.
[16] Huang L, et al. Molecular simulation of adsorption behaviors of methane, carbon dioxide and their mixtures on kerogen: effect of kerogen maturity and moisture content. Fuel 2018;211:159–72.
[17] Xiong F, et al. Pore structure of transitional shales in the Ordos Basin, NW China: effects of composition on gas storage capacity. Fuel 2017;206:504–15.
[18] Ji L, et al. Experimental investigation of main controls to methane adsorption in clay-rich rocks. Appl Geochem 2012;27(12):2533–45.
[19] Busch A, Gensterblum Y. CBM and CO2-ECBM related sorption processes in coal: a

review. Int J Coal Geol 2011;87(2):49–71.
[20] Jin Z, Firoozabadi A. Methane and carbon dioxide adsorption in clay-like slit pores by Monte Carlo simulations. Fluid Phase Equilib 2013;360:456–65.
[21] Tian Y, Yan C, Jin Z. Characterization of methane excess and absolute adsorption in various clay nanopores from molecular simulation. Sci Rep 2017;7(1):12040.
[22] Li J, et al. Water distribution characteristic and effect on methane adsorption capacity in shale clay. Int J Coal Geol 2016;159:135–54.
[23] Zhou S, et al. Experimental study of supercritical methane adsorption in Longmaxi shale: insights into the density of adsorbed methane. Fuel 2018;211:140–8.
[24] Tian H, et al. Characterization of methane adsorption on overmature Lower Silurian-Upper Ordovician shales in Sichuan Basin, southwest China: experimental results and geological implications. Int J Coal Geol 2016;156:36–49.
[25] Tang X, et al. Thermodynamic analysis of high pressure methane adsorption in Longmaxi shale. Fuel 2017;193:411–8.
[26] Zhao H, Wu T, Firoozabadi A. High pressure sorption of various hydrocarbons and carbon dioxide in Kimmeridge Blackstone and isolated kerogen. Fuel 2018;224:412–23.
[27] Zhao H, Lai Z, Firoozabadi A. Sorption hysteresis of light hydrocarbons and carbon dioxide in shale and Kerogen. Sci Rep 2017;7(1):16209.
[28] Zhong J, et al. Experimental study of the impact on methane adsorption capacity of continental shales with thermal evolution. J Nat Gas Geosci 2016;1(2):165–72.
[29] Zhou S, et al. Difference between excess and absolute adsorption capacity of shale and a new shale gas reserve calculation method. Nat Gas Ind 2016;36(11):12–20.
[30] Lu X-C, Li F-C, Watson AT. Adsorption measurements in Devonian shales. Fuel 1995;74(4):599–603.
[31] Myers AL, Monson PA. Physical adsorption of gases: the case for absolute adsorption as the basis for thermodynamic analysis. Adsorption 2014;20(4):591–622.
[32] Mertens FO. Determination of absolute adsorption in highly ordered porous media. Surf Sci 2009;603(10–12):1979–84.
[33] Li Z, Jin Z, Firoozabadi A. Phase behavior and adsorption of pure substances and mixtures and characterization in nanopore structures by density functional theory. SPE J 2014;19(06):1096–109.
[34] Heller R, Zoback M. Adsorption of methane and carbon dioxide on gas shale and pure mineral samples. J Unconventional Oil Gas Resour 2014;8:14–24.
[35] Ren W, et al. Adsorption and surface diffusion of supercritical methane in shale. Ind Eng Chem Res 2017;56(12):3446–55.
[36] Tsai MC, et al. Adsorption of gas mixture on activated carbon. Carbon 1985;23(2):167–73.
[37] Lewis WK, et al. Pure gas isotherms. Ind Eng Chem 1950;42(7):1326–32.
[38] Grant RJ, Manes M. Correlation of some gas adsorption data extending to low pressures and supercritical temperatures. Ind Eng Chem Fundam 1964;3(3):221–4.
[39] Zhang J, et al. Methane and carbon dioxide adsorption on illite. Energy Fuels 2016;30(12):10643–52.
[40] Didar BR, Akkutlu IY. Pore-size dependence of fluid phase behavior and properties in organic-rich shale reservoirs. SPE International Symposium on Oilfield Chemistry. Society of Petroleum Engineers; 2013.
[41] Cristancho-Albarracin D, et al. Shale gas storage in kerogen nanopores with surface heterogeneities. Appl Geochem 2017;84:1–10.
[42] Langmuir I. The constitution and fundamental properties of solids and liquids Part I. Solids. J the Am Chem Soc 1916;38(11):2221–95.
[43] Gensterblum Y, et al. High-pressure CH4 and CO2 sorption isotherms as a function of coal maturity and the influence of moisture. Int J Coal Geol 2013;118:45–57.
[44] Benard P, Chahine R. Determination of the adsorption isotherms of hydrogen on activated carbons above the critical temperature of the adsorbate over wide temperature and pressure ranges. Langmuir 2001;17(6):1950–5.
[45] Dubinin M. Porous structure and adsorption properties of active carbons. Chem Phys Carbon 1966;9:51–119.
[46] Dubinin MI. Physical adsorption of gases and vapors in micropores. Progress in Surface and Membrane Science. Elsevier; 1975. p. 1–70.
[47] Chen S, Yang R. Theoretical basis for the potential theory adsorption isotherms. The Dubinin-Radushkevich and Dubinin-Astakhov equations. Langmuir 1994;10(11):4244–9.
[48] Sakurovs R, et al. Application of a modified Dubinin－Radushkevich equation to adsorption of gases by coals under supercritical conditions. Energy Fuels 2007;21(2):992–7.
[49] Ono S, Kondo S. Molecular theory of surface tension in liquids. Structure of Liquids/Struktur der Flüssigkeiten. Springer; 1960. p. 134–280.
[50] Aranovich GL, Donohue MD. Adsorption isotherms for microporous adsorbents. Carbon 1995;33(10):1369–75.
[51] Aranovich GL, Donohue MD. Adsorption of supercritical fluids. J Colloid Interface Sci 1996;180(2):537–41.
[52] Aranovich G, Donohue M. Predictions of multilayer adsorption using lattice theory. J Colloid Interface Sci 1997;189(1):101–8.
[53] Aranovich G, Donohue M. Vapor adsorption on microporous adsorbents. Carbon 2000;38(5):701–8.
[54] Bi H, et al. The Ono-Kondo model and an experimental study on supercritical adsorption of shale gas: a case study on Longmaxi shale in southeastern Chongqing, China. J Nat Gas Sci Eng 2016;35:114–21.
[55] Huo P, et al. CO_2 geological sequestration: displacement behavior of shale gas methane by carbon dioxide injection. Int J Greenhouse Gas Control 2017;66:48–59.
[56] Zhang D-F, et al. Supercritical pure methane and CO_2 adsorption on various rank coals of China: experiments and modeling. Energy Fuels 2011;25(4):1891–9.
[57] Chalmers GR, Bustin RM, Power IM. Characterization of gas shale pore systems by porosimetry, pycnometry, surface area, and field emission scanning electron microscopy/transmission electron microscopy image analyses: examples from the Barnett, Woodford, Haynesville, Marcellus, and Doig units. AAPG Bull 2012;96(6):1099–119.
[58] Curtis ME, et al. Development of organic porosity in the Woodford Shale with increasing thermal maturity. Int J Coal Geol 2012;103:26–31.
[59] Jin Z, Firoozabadi A. Phase behavior and flow in shale nanopores from molecular simulations. Fluid Phase Equilib 2016;430:156–68.
[60] Jin Z. Bubble/dew point and hysteresis of hydrocarbons in nanopores from molecular perspective. Fluid Phase Equilib 2018;458:177–85.
[61] Orendt AM, et al. Three-dimensional structure of the Siskin Green River Oil Shale Kerogen Model: a comparison between calculated and observed properties. Energy Fuels 2013;27(2):702–10.
[62] Ungerer P, Collell J, Yiannourakou M. Molecular modeling of the volumetric and thermodynamic properties of kerogen: influence of organic type and maturity. Energy Fuels 2014;29(1):91–105.
[63] Bousige C, et al. Realistic molecular model of kerogen's nanostructure. Nat Mater 2016;15(5):576.
[64] Zhou S. Comments on paper "the shale gas sorption capacity of transitional shales in the Ordos Basin, NW China". Fuel 2017.
[65] Benard P, Chahine R. Modeling of high-pressure adsorption isotherms above the critical temperature on microporous adsorbents: application to methane. Langmuir 1997;13(4):808–13.
[66] Sudibandriyo M, et al. Ono-Kondo lattice model for high-pressure adsorption: pure gases. Fluid Phase Equilib 2010;299(2):238–51.
[67] Merey S, Sinayuc C. Gas-in-place calculations in shale gas reservoirs using experimental adsorption data with adsorption models. Can J Chem Eng 2016;94(9):1683–92.
[68] Merey S, Sinayuc C. Analysis of carbon dioxide sequestration in shale gas reservoirs by using experimental adsorption data and adsorption models. J Nat Gas Sci Eng 2016;36:1087–105.
[69] Martin MG, Siepmann JI. Transferable Potentials for Phase Equilibria. 1. United-Atom Description of n-Alkanes. J Phys Chem B 1998;102(14):2569–77.
[70] Talu O, Myers AL. Reference potentials for adsorption of helium, argon, methane, and krypton in high-silica zeolites. Colloids Surf, A 2001;187–188:83–93.
[71] Steele WA. The physical interaction of gases with crystalline solids: I. Gas-solid energies and properties of isolated adsorbed atoms. Surf Sci 1973;36(1):317–52.
[72] Widom B. Some topics in the theory of fluids. J Chem Phys 1963;39(11):2808–12.
[73] Metropolis N, et al. Equation of state calculations by fast computing machines. J Chem Phys 1953;21(6):1087–92.
[74] Chen G, et al. Keys to linking GCMC simulations and shale gas adsorption experiments. Fuel 2017;199:14–21.
[75] Mosher K, et al. Molecular simulation of methane adsorption in micro-and mesoporous carbons with applications to coal and gas shale systems. Int J Coal Geol 2013;109:36–44.
[76] Chen G, et al. Adsorption behavior of hydrocarbon on Illite. Energy Fuels 2016;30(11):9114–21.
[77] Chen G, et al. Research of CO_2 and N_2 adsorption behavior in K-Illite Slit Pores by GCMC method. Sci Rep 2016;6:37579.
[78] Ambrose RJ, et al. Shale gas-in-place calculations part I: new pore-scale considerations. SPE J 2012;17(01):219–29.
[79] Li Z, Cao D, Wu J. Layering, condensation, and evaporation of short chains in narrow slit pores. J Chem Phys 2005;122(22):224701.
[80] Luo X, et al. Adsorption of methane, carbon dioxide and their binary mixtures on Jurassic shale from the Qaidam Basin in China. Int J Coal Geol 2015;150:210–23.
[81] Sakurovs R, et al. Application of a modified Dubinin－ Radushkevich equation to adsorption of gases by coals under supercritical conditions. Energy Fuels 2007;21(2):992–7.
[82] Do D, Do H. Adsorption of supercritical fluids in non-porous and porous carbons: analysis of adsorbed phase volume and density. Carbon 2003;41(9):1777–91.
[83] Do D, et al. On the existence of negative excess isotherms for argon adsorption on graphite surfaces and in graphitic pores under supercritical conditions at pressures up to 10,000 atm. Langmuir 2010;26(7):4796–806.
[84] Jin Z. Effect of nano-confinement on high pressure methane flow characteristics. J Nat Gas Sci Eng 2017;45:575–83.